Swimming dynamics of bidirectional artificial flagella

Namdeo, S.; Khaderi, S. N.; Onck, P. R.

Published in:
Physical Review E

DOI:
10.1103/PhysRevE.88.043013

Publication date:
2013

Swimming dynamics of bidirectional artificial flagella

S. Namdeo,[1] S. N. Khaderi,[2] and P. R. Onck[1,*]

[1]*Zernike Institute for Advanced Materials, University of Groningen, 9747 AG Groningen, The Netherlands*

[2]*Department of Engineering, University of Cambridge, Cambridge CB2 1PZ, England, United Kingdom*

(Received 8 August 2013; revised manuscript received 25 September 2013; published 25 October 2013)

We study magnetic artificial flagella whose swimming speed and direction can be controlled using light and magnetic field as external triggers. The dependence of the swimming velocity on the system parameters (e.g., length, stiffness, fluid viscosity, and magnetic field) is explored using a computational framework in which the magnetostatic, fluid dynamic, and solid mechanics equations are solved simultaneously. A dimensionless analysis is carried out to obtain an optimal combination of system parameters for which the swimming velocity is maximal. The swimming direction reversal is addressed by incorporating photoresponsive materials, which in the photoactuated state can mimic natural mastigonemes.

DOI: 10.1103/PhysRevE.88.043013 PACS number(s): 47.63.−b, 87.85.−d, 02.70.−c, 47.90.+a

I. INTRODUCTION

A rapidly growing field in biotechnology is the fabrication of microfluidic or laboratory-on-a-chip devices for biomedical applications. For a successful future implementation of these devices, it is important that one is able to accurately move and position micro-objects (e.g., cells and organelles) within the device [1]. In addition, for targeted drug delivery applications, microswimmers have been proposed that transport drug-containing vesicles to specific regions in the body using external triggers [2]. The primary challenge in designing a micrometer- or nanometer-size swimmer is that the motion of the swimmer should be nonreciprocal (time irreversible) in nature as described by Purcell in the "scallop theorem" [3]. This theorem states that a scallop executing a time reversible or reciprocal motion (i.e., the forward motion is the same as the backward motion in space and time) will not be able to swim in the Stokes regime [3]. This is due to the fact that at these small length scales, fluid dynamics is dominated by viscous forces rather than inertial forces (low Reynolds numbers) [3,4]. As a result, researchers have tried to mimic the swimming strategies of flagellated micro-organisms [5] (e.g., bacteria and spermatozoa), which are able to generate a nonreciprocal motion by the use of hairlike projections known as flagella [2,4,6–10]. For instance, Dreyfus *et al*. [6] have used a DNA-linked magnetic colloidal chain, which can be actuated using an external magnetic field, mimicking the swimming of spermatozoa [see Fig. 1(a)].

To explore and exploit the propulsion capabilities of flagella, the swimming dynamics of externally actuated flexible filaments has been analyzed analytically [12–17] and experimentally [18] in the literature. Efforts have also been made to experimentally investigate swimming of a magnetically actuated centimeter-size flexible film attached to a magnetic head [19,20]. The filaments or films move forward by pushing the surrounding fluid during their bending motion and the swimming dynamics is driven by the undulating motion of the elastica in a viscous medium. However, many of the suggested microswimmers cannot reverse their swimming direction, which is an important asset of micro-object manipulation, particularly in confined flow geometries. Interestingly, micro-organisms exist in nature (e.g., ochrophytes) that have flagella covered with vertical appendages (called mastigonemes) [21–24]. A flagellum bearing mastigonemes is known to swim in a direction opposite to that of a smooth flagellum [21–25]. In this article, we adopt this mechanism to develop a bioinspired bidirectional swimmer by combining the swimming principles of a smooth flagellum and a flagellum with mastigonemes. To control the swimming speed and direction, we employ two different responsive materials that can be externally actuated using magnetism [2,6,8–10,18–20,26–28] and light [29–31]. We study the swimming dynamics of such a microswimmer using a solid-fluid interaction model and explore the underlying physics using dimensionless parameters.

II. COMPUTATIONAL MODEL AND DIMENSIONAL ANALYSIS

Analyzing the swimming of a magnetically actuated microswimmer [a conceptual design is shown in Fig. 1(b)] requires a computational model that accounts for the fluid-solid interaction (FSI) between the deforming swimmer and the surrounding fluid, while properly incorporating the changing magnetic forces imposed by the applied magnetic field. To do so, we use a two-dimensional (2D) computational framework in which the magnetostatic, fluid dynamics, and solid mechanics equations are simultaneously solved using the finite-element method. Although the flow around an oscillating flagellum is intrinsically three dimensional in nature, here we consider a model system to explore the underlying physics associated with flagellar propulsion and plausible means to achieve swimming direction reversal. Our analysis is similar to the analysis performed by Taylor [32], in which the swimming of an infinite sheet has been analyzed. The obtained swimming velocity was shown to have a similar (qualitative) dependence on the flagellar wave parameters compared to experimental observations [32,33] and to three-dimensional theoretical approaches [34–37]. A similar design, as shown schematically in Fig. 1(b) (a floppy film attached to a magnetic head), has been analyzed experimentally at the millimeter length scale [19,20].

*P.R.Onck@rug.nl

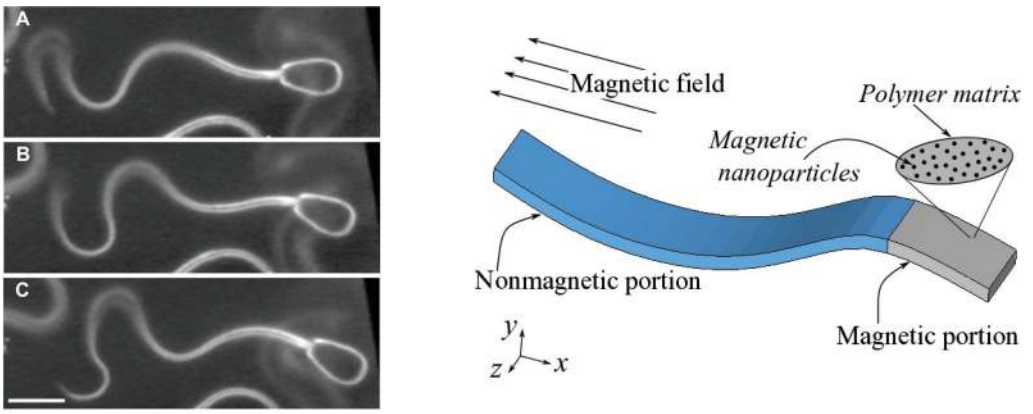

FIG. 1. (Color online) (a) Three video-fields (A–C), successively 200 ms apart, showing bend propagation in a spermatozoon [11]. The scale bar is 10 μm. [Figures are reproduced with permission of the copyright owner(s).] (b) Conceptual design illustration of a magnetic microswimmer with the magnetic portion consisting of a polymer matrix embedded with magnetic nanoparticles such that it can be actuated through an oscillatory external magnetic field.

We follow the same approach as in Ref. [27], where we linearize and discretize the principle of virtual work to arrive at the final set of equations by adopting an updated Lagrangian framework. The microswimmer is represented by a collection of 2D beam elements, which act as an internal boundary to the fluid domain. A monolithic approach is used to couple the Lagrangian formulation of the solid to the Eulerian formulation of the fluid, where we incorporate the fluid drag forces using the method of Lagrange multipliers [38]. During the simulations the external magnetic actuation leads to the generation of magnetic body couples that are considered as an external force vector to the FSI model. The magnetic body couples are obtained by solving the Maxwell equations for the magnetostatic problem with no free currents [39]. Using dimensional analysis, it can be shown that the system parameters [e.g., length, thickness, stiffness, fluid viscosity, and magnetic field; see Fig. 2(a)] can be captured in terms of the following set of dimensionless parameters: (i) the fraction of film that is magnetic

$$L_0/L, \tag{1}$$

(ii) the magnetic number

$$M_n = 12B_{ext}^2 L L_0/\mu_0 E h^2, \tag{2}$$

and (iii) the fluid number

$$F_n = 12\mu L^3/E h^3 t_{ref}, \tag{3}$$

where L_0 is the magnetic portion of the elastica characterized by the magnetic susceptibility tensor $\boldsymbol{\chi}$, L and h are the length and thickness of the film, respectively, E is Young's modulus, μ is the viscosity of the fluid, t_{ref} is the cycle time of the magnetic field oscillation, B_{ext} is the magnitude of the applied magnetic field, and μ_0 is the permeability of free space. Note that we have one length parameter L_0/L defining the normalized length of the magnetic portion in the elastica and

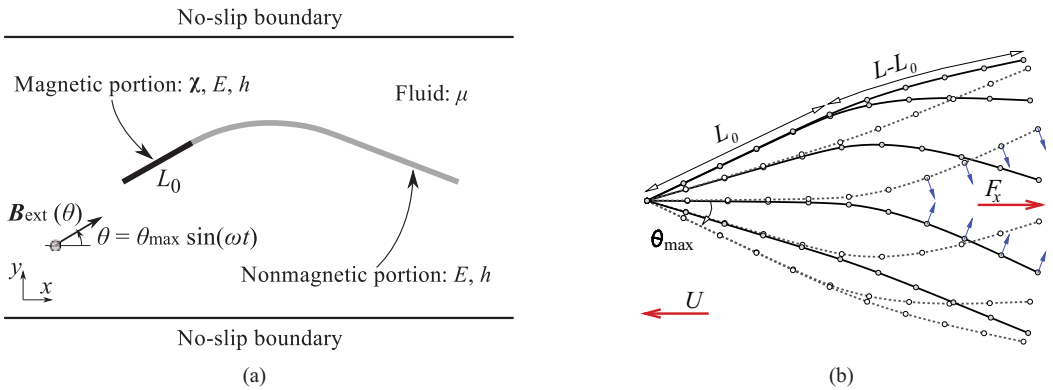

FIG. 2. (Color online) (a) Partially magnetized elastica (PME) of functional polymers under an external magnetic field $\boldsymbol{B}_{ext}$, where the magnetic portion is characterized by the length L_0 and the magnetic susceptibility tensor $\boldsymbol{\chi}$. Furthermore, h and E are the thickness and Young's modulus of the elastica, respectively, while μ is the viscosity of the fluid. The solid-fluid interaction induces bending deformations during the magnetic actuation as illustrated. (b) Steady-state nonreciprocal motion of the magnetically actuated PME for $L_0 = 0.5L$. The solid lines represent the upward motion (from $-\theta_{max}$ to θ_{max}) and the dashed lines represent the downward motion (from θ_{max} to $-\theta_{max}$). Note that the induced bending curvature changes sign during the actuation cycle leading to propulsion of the PME. All configurations are translated such that the left ends of the PME meet at one point. An animation of the PME's forward swimming is included in Ref. [40].

two force parameters obtained through normalization with the elastic forces, namely, the magnetic number M_n, defining the ratio of magnetic to elastic forces, and the fluid number F_n, defining the ratio of fluid to elastic forces.[1] The computational framework and dimensional analysis are briefly summarized in the Appendix; for full details of the approach and validation studies the reader is referred to Ref. [27].

III. RESULTS AND DISCUSSION

The microswimmer consists of a functional polymer film, which is partially magnetic (using embedded superparamagnetic nanoparticles), such that it can be actuated through an oscillatory external magnetic field [see Fig. 2(a)]. The magnetic field at any time instant t is $\boldsymbol{B}_{\text{ext}} = B_{\text{ext}}\cos(\theta)\boldsymbol{i} + B_{\text{ext}}\sin(\theta)\boldsymbol{j}$, where B_{ext} is the magnitude of the field, $\boldsymbol{i}$ and $\boldsymbol{j}$ are the unit vectors in the coordinate directions, and $\theta = \theta_{\max}\sin(\omega t)$, with $\theta_{\max}$ the maximum rotational angle for the magnetic field vector $\boldsymbol{B}_{\text{ext}}$ and $\omega = 2\pi/t_{\text{ref}}$ the frequency of the applied magnetic field, where t_{ref} is the cycle time. Note that the magnetic field oscillates between the angles $-\theta_{\max}$ and $\theta_{\max}$ [see Fig. 2(a)]. The length and thickness of the polymer film are L and h, respectively, and the magnetic portion of the film has length L_0. The microswimmer, which we termed partially magnetized elastica (PME), is placed in the center of a microfluidic channel, where both the width and height of the channel are twice the microswimmer's length L. The microfluidic channel is represented by no-slip top and bottom boundaries, while the left and right are considered as free boundaries. For the simulations, the microswimmer is discretized using 40 equal-size beam elements and the fluid domain is divided into 30×30 elements [27], which ensure numerical convergence of the results. Furthermore, we take $h/L = 1/100$ and $\theta_{\max} = 26.57^\circ$ and the tangential and normal magnetic susceptibilities are assumed to be $\chi_t = 4.6$ and $\chi_n = 0.8$, respectively [27]. The rest of the parameters will be specified through the three dimensionless quantities L_0/L, F_n, and M_n.

A. Unidirectional swimming using magnetic actuation

During magnetic actuation, the orientation of the magnetic portion follows the external magnetic field $\boldsymbol{B}_{\text{ext}}$ and due to the viscous resistance of the fluid, bending deformations are induced in the nonmagnetic portion of the PME [see Fig. 2(a)]. As a result, the microswimmer pushes the fluid to the right with a net force F_x, causing a swimming velocity U to the left [see Fig. 2(b) and Ref. [40]]. In the following, we will study how the swimming velocity depends on the film properties and magnetic field parameters. Note that the propulsive dynamics of an end-actuated flexible filament has been extensively analyzed in the literature [7,12–18]. However, any practical implementation requires a finite-size magnetic object (head) to be attached to the flexible film (filament). Here we aim to explore this effect by studying the role of L_0/L on the swimming dynamics. To do so, we start out by exploring the hydrodynamic origin of the swimming dynamics in some more detail by looking at the system from a fluid propulsion (Lagrangian) point of view. For this, we analyze a nonpropelling PME by fixing the lateral and transverse motions of the magnetic tip while rotations are allowed (hinged boundary condition). Figure 3 shows the steady-state nonreciprocal motion at various time instances for $L_0 = 0.5L$, in addition to the applied magnetic field $\boldsymbol{B}_{\text{ext}}$, contours of horizontal fluid velocity, and streamlines indicating the direction of the velocity. Note that the bending curvature changes sign during the upward and downward strokes, which breaks the time symmetry, leading to propulsion. The magnetically actuated (magnetic) portion of the PME remains rigid (under the influence of the magnetic field) while it rotates and follows the external magnetic field (see Fig. 3). During both the upward and downward strokes the microswimmer pushes the fluid to the right as indicated in Fig. 3. For a propelling PME, the similar undulating motion is observed as shown in Fig. 2(b), where all configurations are translated such that the left ends of the PME meet at one point.

Next we analyze the swimming velocity of the PME as a function of the dimensionless parameters derived in Sec. II. For a given value of F_n the influence of the other dimensionless parameters are shown in Fig. 4 with the swimming velocity U being normalized with L/t_{ref}. It is interesting to note that $L_0/L = 0$ and 1 represent two extreme cases for which the swimming velocity will be zero, either due to the lack of external actuation ($L_0 = 0$) or due to reciprocal motion ($L_0 = L$). The simulation results demonstrate that for a given value of F_n the swimming velocity reaches a maximum for $0 < (L_0/L)_{\text{opt}} < 1$ as shown in Fig. 4. The optimal value $(L_0/L)_{\text{opt}}$ (i.e., the L_0/L value that leads to maximal velocity for a given F_n) is found to be (monotonically) increasing with F_n. In addition, for given values of L_0/L and F_n, the swimming velocity increases initially with M_n and saturates for higher M_n values, which is related to the fact that the magnetic portion of the PME becomes fully responsive to the applied magnetic field at high M_n values by overcoming the viscous resistance of the surrounding fluid. Obviously, the M_n value required to achieve a fully responsive microswimmer depends on the value of F_n and it was observed that the PME becomes fully responsive when $M_n > 70F_n$. For the cases when $L_0/L > (L_0/L)_{\text{opt}}$ a local peak in the swimming velocity is observed, which is followed by a decline and eventually a saturation for higher M_n values (see Fig. 4). This is related to the viscous drag-induced deformation of the magnetic portion, which is prominent for small M_n and thus contributes to the propulsion. However, when the magnetic field increases, the magnetic portion of the film becomes more and more rigid, leading to a reduced portion of the swimmer (i.e., $L - L_0$) that contributes to the nonreciprocal deformation. For the fully responsive microswimmers ($M_n > 70F_n$), the normalized swimming velocity ($U^* = Ut_{\text{ref}}/L$) as a function of F_n and L_0/L is shown in Fig. 5. The maximum swimming velocity associated with $(L_0/L)_{\text{opt}}$ is highlighted with white dots for all given values of F_n. The swimming velocity is maximal

[1]The definition of the fluid number F_n is similar to the "sperm number" $S_p = (\frac{L^4\mu\omega}{EI})^{1/4}$ defined by Lowe [13] and is used as a nondimensional length parameter by other researchers [7,12,14–18]. It can be shown that for the partially magnetized elastica, $F_n = \frac{S_p^4 b}{2\pi L}$.

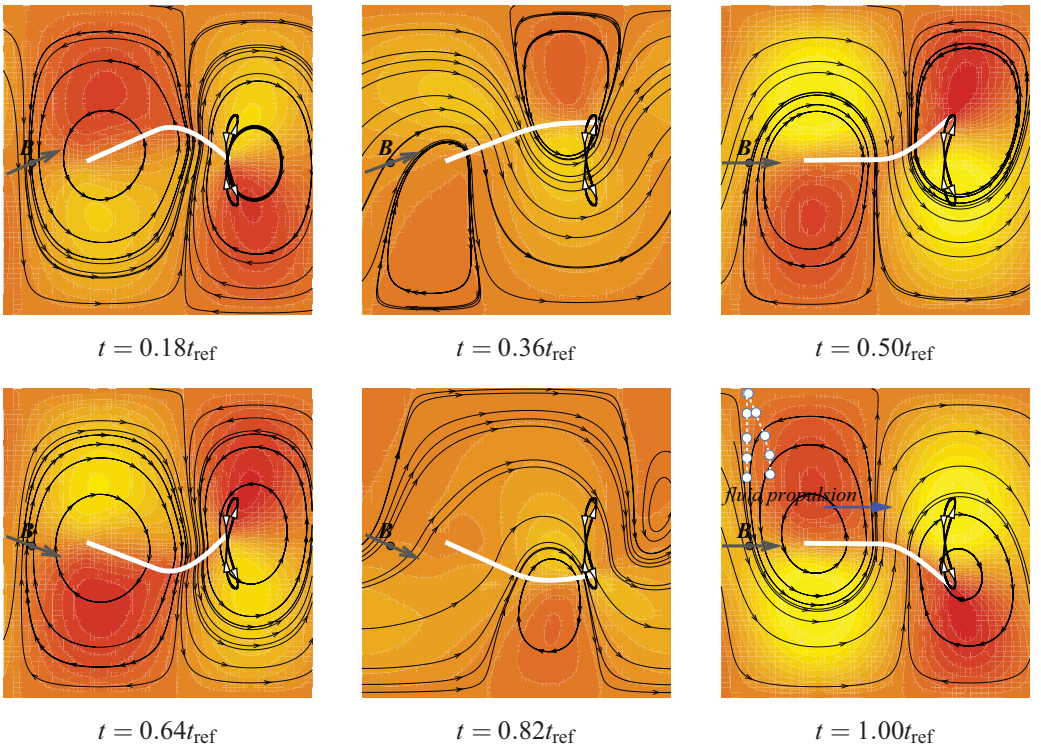

FIG. 3. (Color online) Steady-state nonreciprocal motion of the magnetically actuated PME for $L_0 = 0.5L$. The contours represent the horizontal velocity of the fluid [dark (red) and light (yellow) colors represent velocities of 15 and -15 mm/s, respectively]. At various time instances the applied magnetic field and the streamlines indicating the direction of the velocity are shown. The fluid particles are pushed to the right, as indicated by the last figure after one actuation cycle. Note that there is a gradient in the fluid particle velocity due to the presence of the no-slip boundary conditions at the top and bottom surfaces of the microfluidic channel. The nonzero area swept by the PME's right tail is shown with the solid black line, which is an indication of nonreciprocal motion. The PME is constrained not to swim by fixing the lateral and transverse motions of the left magnetic tip, while rotations are allowed (hinged boundary condition).

$(U^* = 59.4 \times 10^{-3})$ for $F_{\mathrm{n}} = 1.5$ with a corresponding value of $(L_0/L)_{\mathrm{opt}} = 0.55$.

The swimming velocity depends on the nonreciprocal motion executed by the PME in the presence of a viscous medium. The deformed shape of the magnetically actuated PME at various values of L_0/L and F_{n} is shown in Fig. 6. By correlating the deformed shapes of the PME to their respective swimming velocities shown in Fig. 5, it can be noted that short nonmagnetic tails [e.g., $L_0/L > (L_0/L)_{\mathrm{opt}}$] at small F_{n} values as well as long nonmagnetic tails [e.g., $L_0/L < (L_0/L)_{\mathrm{opt}}$] at large F_{n} values are inefficient in creating a net forward propulsion. In the case of short tails, the PME mostly executes a reciprocal motion, while in the case of long tails, the PME motion is hindered due to excessive drag [7,12,14–18]. Clearly, for low F_{n} values the optimal L_0/L is small in order to maximize the bending deformations in the nonmagnetic portion, while for large F_{n} values the optimal L_0/L is large to generate appreciable oscillation amplitudes.

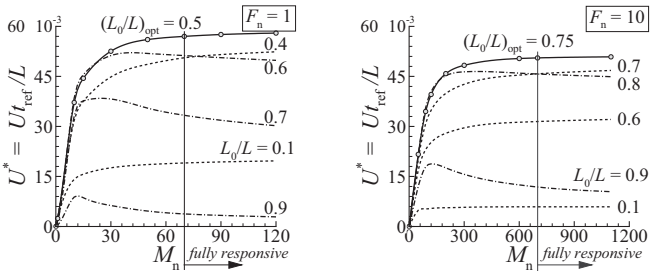

FIG. 4. Swimming velocity as a function of M_{n} and L_0/L for a given value of F_{n}. For all values of F_{n}, the swimming velocity is maximal for $(L_0/L)_{\mathrm{opt}}$ and the $(L_0/L)_{\mathrm{opt}}$ value is monotonically increasing with F_{n}. In addition, for all values of $(L_0/L)_{\mathrm{opt}}$ (corresponding to specific F_{n} values) the swimming velocity saturates when $M_{\mathrm{n}} > 70F_{\mathrm{n}}$ as the microswimmer becomes fully responsive to the applied magnetic field (see the text). The solid lines correspond to $L_0/L = (L_0/L)_{\mathrm{opt}}$, while the dashed and dash-dotted lines correspond to $L_0/L < (L_0/L)_{\mathrm{opt}}$ and $L_0/L > (L_0/L)_{\mathrm{opt}}$, respectively.

Swimming of (end-) actuated flexible filaments of finite length has been analyzed in the literature [7,12–18], where it has been shown that the optimal length of the filament scales with a characteristic viscous penetration length, defined by $l_\eta = (EI/\mu\omega)^{1/4}$, with I being the second moment of area. Using this result, we can approximate the optimal length of the nonmagnetic portion to scale with $L/F_{\mathrm{n}}^{1/4}$ because $F_{\mathrm{n}} \propto \mu\omega/EI$. Since the PME can be considered as an end-actuated elastica of length $L - L_0$ (the nonmagnetic portion of the film), we can write $(L - L_0)_{\mathrm{opt}} = CL/F_{\mathrm{n}}^{1/4}$, where the proportionality constant C has to be determined. Using one sample simulation result [i.e., for $F_{\mathrm{n}} = 1$ the optimal magnetic

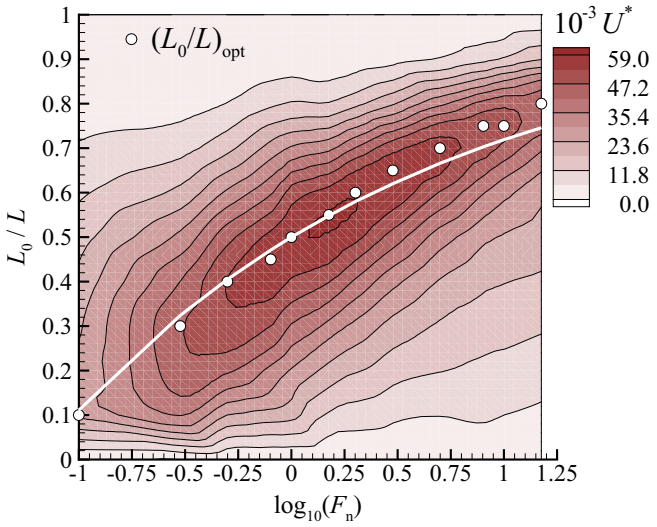

FIG. 5. (Color online) Normalized swimming velocity $U^* = Ut_{ref}/L$ as a function of F_n and L_0/L for fully responsive microswimmers ($M_n > 70F_n$). The white dots represent the maximum swimming velocity associated with $(L_0/L)_{opt}$ for a given value of F_n. The swimming velocity is maximal for $F_n = 1.5$ and the corresponding value of $(L_0/L)_{opt} = 0.55$. The analytical prediction of $(L_0/L)_{opt}$ as a function of F_n, $(L_0/L)_{opt} = 1 - 0.5/F_n^{1/4}$, is shown by the white line; see the text for details.

portion is $(L_0/L)_{opt} = 0.5$] we obtain $C = 0.5$, giving the relation $(L_0/L)_{opt} = 1 - 0.5/F_n^{1/4}$, which is in accordance with the simulation results as shown in Fig. 5.

Next we perform a simple analytical study for the PME propulsion, where we attempt to capture the functional dependence of the optimal swimming velocity on the dimensionless parameters as shown in Fig. 5 for fully responsive microswimmers. The fully responsive PME motion demonstrates a typical first mode of oscillations as shown in Figs. 2(b) and 3, which can be decomposed into two individual reciprocal motions that beat out of phase, with the first reciprocal motion representing a rigid-body rotation (due to the magnetic actuation) and the second a nonlinear cyclic deformation (due to the fluid drag). Interestingly, the interaction of these two individual reciprocal motions would lead to a nonreciprocal motion (the oar motion), which can be represented by a simple mathematical expression given by

$$y(x,t) = \underbrace{a_1 \sin(\omega t)(x/L)}_{\text{term 1}} + \underbrace{a_2 \sin(\omega t + \Phi)(x/L)^m}_{\text{term 2}}, \quad (4)$$

where Φ is the phase lag, a_1 dictates the amplitude of the rigid-body rotation, and a_2 and m dictate the amplitude and curvature associated with the fluid-induced bending deformations of the nonmagnetic portion, governed by F_n and $L - L_0$.

Now the resistive force theory suggested by Gray and Hancock [34] can be used to get a first-order approximation of the swimming velocity associated with the oar motion mathematically represented by Eq. (4). Assuming the local drag coefficients (per unit length) for a microswimmer to be C_n and C_t in the normal and tangential directions, respectively, the x component of the total force on the microswimmer of length L can be written as [34]

$$F_x = \int_0^L C_t \left\{ \left(\frac{C_n}{C_t} - 1 \right) \frac{dy}{dt}\frac{dy}{dx} - U \right\} ds = 0. \quad (5)$$

Note that the above expression is derived assuming that the microswimmer is swimming with a velocity U. The total

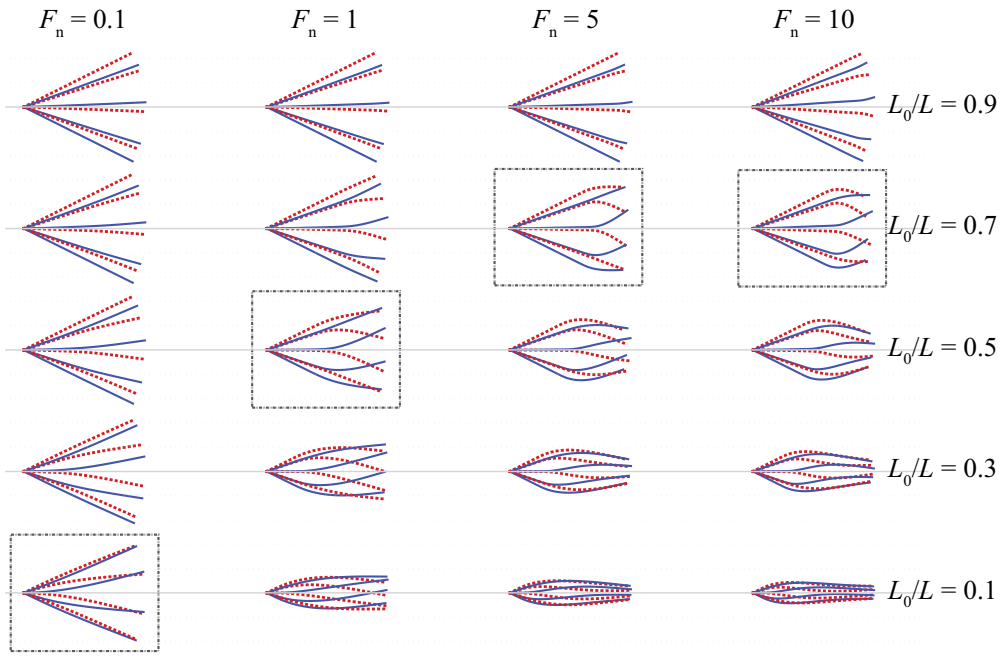

FIG. 6. (Color online) Deformed shape of the magnetically actuated PME at various values of L_0/L and F_n and for $M_n > 70F_n$. The dotted (red) and solid (blue) lines represent the upward and downward motion of the PME, respectively. All configurations are translated such that the left ends of the PME meet at one point. For a given value of F_n the optimal PME's configurations are highlighted by an enclosed box [note that $(L_0/L)_{opt} = 0.75$ for $F_n = 10$].

force consists of a propulsive part due to the nonreciprocal motion [first term of the integrand in Eq. (5)] and a retarding part due to the drag forces opposing the horizontal swimming velocity [the second term in Eq. (5)]. When the microswimmer reaches a steady-state swimming velocity U, the propulsive and retarding forces are in (dynamic) equilibrium, so the total force must be zero [25]. By substituting Eq. (4) into Eq. (5) the swimming velocity can be calculated to be

$$U = \pi\,(C_n/C_t - 1)\,a_1 a_2 \sin(\Phi)(m-1)/(m+1)Lt_{\mathrm{ref}}. \quad (6)$$

This expression clearly emphasizes the need of a phase difference between two (reciprocal) degrees of freedom associated with a microswimmer in order to generate a nonreciprocal motion and the associated nonzero swimming velocity [3,41]. Similar arguments have been given for two hydrodynamically interacting scallops individually executing a reciprocal motion [42]. The swimming velocity will be maximum for a phase difference of $\pm\pi/2$ and can be reversed by reversing the sign of the phase difference (discussed in the next section).

For the PME motion the induced bending curvature due to the fluid drag indicates $m > 1$ and a phase difference $\Phi \simeq -\pi/2$, which are governed by the viscous forces and cannot be externally controlled (i.e., the PME cannot reverse the swimming direction). By comparing the actual PME motion with Eq. (4) for the cases of optimal swimming velocities, the parameters of Eq. (4) were found to depend on the PME system parameters through $a_1 = L\sin(\theta_{\max})$, $a_2 \sin(\Phi) \propto L_0(1 - L_0/L)$, and $m = 1 + 10L_0/L$, where m controls the portion of the film involved in the induced bending curvature, which is governed by L_0/L. Substitution in Eq. (6) yields

$$U^*_{\mathrm{opt}} = U_{\mathrm{opt}}(t_{\mathrm{ref}}/L) \propto L_0^2(L - L_0)\sin(\theta_{\max})/(L_0L^2 + 0.2L^3), \quad (7)$$

which is in accordance with the simulation results of Fig. 5, with both simulations and Eq. (7) predicting an overall maximal swimming velocity for $(L_0/L)_{\mathrm{opt}} = 0.55$ and the corresponding value of $F_{\mathrm{n}} = 1.5$ (see Fig. 11).

B. Bidirectional swimming: a conceptual design using magneto- and photoactuation

As explained above, the swimming direction cannot be reversed for the current design of the PME. This is due to the fact that the curvature κ in the nonmagnetic portion is drag induced, which always lags behind the magnetically actuated rigid rotations (θ) of the film (i.e., the phase angle Φ is negative). The associated configurational space [3] for the PME can be illustrated by scenario 1 in Fig. 7, corresponding to $\Phi = -\pi/2$. Note that the configurational space is represented by two degrees of freedom (e.g., κ and θ) and their out-of-phase time sequence necessary to achieve a nonreciprocal motion [3]. Consequently, reversing the time sequence of the configurational degrees of freedom will reverse the swimming direction as schematically depicted by scenario 2 in Fig. 7, corresponding to a phase lag $\Phi = \pi/2$. Although Fig. 7 corresponds to the specific degrees of freedom κ and θ, the sketched scenarios are generic and apply to other microswimmers as well (e.g., Purcell's three-link swimmer [3] or hydrodynamically interacting scallops [42]).

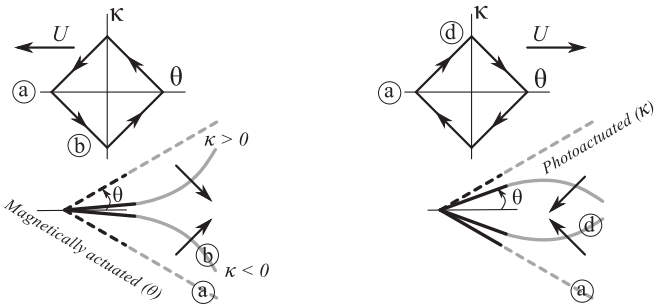

Scenario 1: *forward swimming* Scenario 2: *backward swimming*

FIG. 7. Conceptual design of bidirectional swimming of a magneto- and photoresponsive microswimmer. The associated configurational space indicates the respective values of the angular rotation θ and the curvature κ in the magnetic and nonmagnetic portions of the microswimmer, respectively, along with their actuation sequence. Forward swimming corresponds to a negative phase difference $\Phi = -\pi/2$, while backward swimming corresponds to $\Phi = \pi/2$.

Control of the swimming direction is an important aspect of micro-object manipulation in small flow geometries such as the microchannels in laboratory-on-a-chip devices. In order to endow the PME with bidirectional swimming functionality, an additional independently controlled actuation mechanism is needed to tune the time sequence of the rotation θ and bending κ degrees of freedom. One possibility to achieve this is to use light in order to externally control the bending curvature in the nonmagnetic portion of the PME by means of photoresponsive polymers. It is known that liquid-crystalline polymer films develop a reversible Gaussian curvature upon photoactivation [29–31]. Using such photoresponsive materials along with the magnetoresponsive materials, a bidirectional microswimmer can be designed according to the phase-lag controlled actuation strategy depicted in Fig. 7. Although the above suggested strategy provides a simple design for a bidirectional microswimmer, it requires a complex synchronization of the two independent actuation mechanisms (light and magnetic field). Also, it constrains the actuation frequencies of the magnetic- and light-induced actuations, as well as the associated material response, to be of the same order. However, it is known that the light response of liquid-crystalline polymers is much slower [29–31] compared to the magnetic response of the magnetoresponsive polymers [28], which poses an obvious challenge to the above design.

C. Bidirectional swimming using photoresponsive mastigonemes

Recently, we suggested a bioinspired approach to obtain swimming direction reversal, by referring to the hydrodynamic operation of ochrophytes that feature flagella covered by side appendages, called mastigonemes [25]. In these microorganisms, the mastigonemes work as cilia and cause a reversal in swimming direction compared to a smooth flagellum [25]. It was concluded that the mastigonemes sweep an area in synchrony with the beat cycle of the flagella and push the fluid in the swimming direction of the base flagellum. Basically, the nonzero swept area due to the mastigoneme's motion has to be

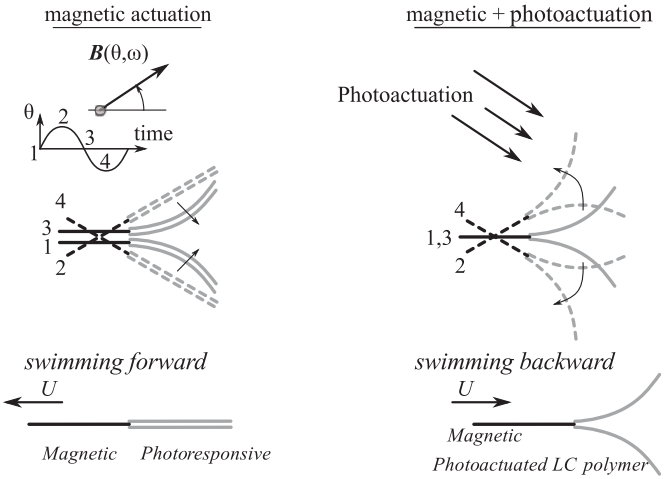

FIG. 8. Illustration of bidirectional swimming of the PME, where the nonmagnetic portion is fabricated with photoresponsive liquid-crystalline (LC) polymers. The forward swimming is achieved by executing a flagellar (oar) motion upon actuation with an external magnetic field; see the left image. To reverse the swimming direction the swimming principle of a flagellum bearing mastigonemes is exploited, where the photoresponsive (nonmagnetic) portions of the microswimmer are photoactuated to form the mastigoneme structures; see the right image.

maximized in order to get an efficient direction reversal [25]. We adopt this mechanism to explore a bioinspired swimmer for which bidirectional swimming is provided by combining the swimming principles of a smooth flagellum and a flagellum bearing mastigonemes. The microswimmer is partially magnetic and mimics the flagellar swimming by executing an oar motion once actuated using an external magnetic field (see the left panel of Fig. 8). Note that the bending deformations are caused by the viscous forces imposed by the fluid, similar to the PME analyzed in Sec. III A. To reverse the swimming direction, the photoresponsive (nonmagnetic) portions of the microswimmer are photoactuated, inducing bending, which mimics the appearance of two mastigonemes (see the right panel of Fig. 8).

Steady-state nonreciprocal motion of such a bidirectional microswimmer is shown in Fig. 9, where we explore the hydrodynamic origin of the swimming direction reversal by looking at the system from a fluid propulsion point of view. Here we analyze a nonpropelling PME by fixing the lateral and transverse motions of the left tip while rotations are allowed (hinged boundary condition). At various time instances the applied magnetic field $\boldsymbol{B}_{\text{ext}}$ and the streamlines indicating the direction of the fluid velocity are shown. The magnetically actuated (magnetic) portion of the PME remains rigid (under the influence of the magnetic field) as it rotates and follows the external magnetic field. In the left column, the forward swimming of the PME is shown, where the PME executes an oar motion upon actuation with an external magnetic field. The nonzero swept area by the tail end is also indicated (the tail sweeps the trace of an eight), which is a measure of the nonreciprocal motion (compare to Fig. 3). During both the upward and downward strokes the microswimmer pushes the fluid to the right as indicated in Fig. 9. In the right column, the swimming direction reversal is shown in the

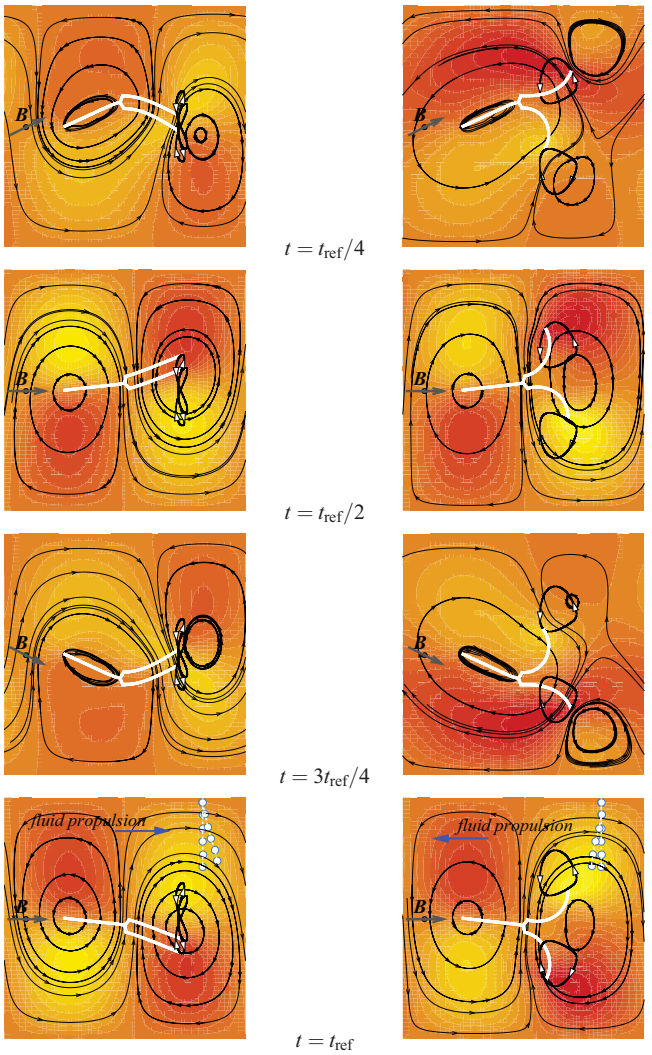

FIG. 9. (Color online) Steady-state nonreciprocal motion of a nonpropelling PME (hinged boundary condition at the left tip) demonstrating the hydrodynamic origin of the swimming direction reversal. The contours represent the horizontal velocity of the fluid [dark (red) and light (yellow) colors represent velocities of 15 and −15 mm/s, respectively]. The direction of the velocity is given by the streamlines and the gray arrowheads represent the applied magnetic field at the respective time instants (indicated in the middle column). The nonzero area swept by the upper and lower appendages of the PME is shown with the arrows indicating the respective direction of motion. The fluid particles are pushed to the right due to the oar motion (see the left column) initially and in the photoactuated state (when the appendages mimic natural mastigonemes) they are pushed to the left (see the right column), as indicated by the bottom figures after one actuation cycle.

photoactuated state, where the nonmagnetic portions of the PME are photoactuated to mimic the mastigonemes. The mastigonemes work as cilia, where the fluid propulsion is achieved due to spatially asymmetric motion during its working cycle consisting of an effective and a recovery stroke [25]. During the effective stroke the cilium stands high and pushes the fluid, while during the recovery stroke, it remains low to limit the back flow, which results in fluid flow in the direction of the effective stroke. It was shown that during

(planar) asymmetric beating of a cilium, a nonzero area is swept by the cilia tip that can be used to quantify the net fluid displaced (a linear relation was found between the swept area and fluid flow) [26]. The area swept by the tip of these mastigonemes is shown with the arrows representing the direction of motion. Interestingly, for the magnetically actuated PME, the upper and lower mastigonemes are synchronized in such a fashion that when the upper mastigoneme executes an effective stroke the lower mastigoneme goes through a recovery stroke and vice versa. This coordinated motion (driven by the magnetic actuation) leads to effectively pushing the fluid to the left as indicated in Fig. 9. For details, the reader is referred to our earlier work [25]. Thus the bidirectional PME swimmer in the nonphotoactuated state executes an oar motion leading to swimming in the forward direction, whereas in the photoactuated state the nonmagnetic portions execute a synchronized ciliary motion (the upper and lower mastigonemes are effectively pushing the fluid alternatively) leading to swimming in the backward direction (see Fig. 9 and Ref. [40]). Interestingly, Chlamydomonas, a genus of green alga, swims by means of synchronous ciliary beating of its two flagella [43,44]. However, it can suddenly change or reverse its swimming direction by generating flagellar beating of its two flagella upon exposure to light or calcium ions [44].

The photoresponse (induced bending curvature) of liquid-crystalline polymer is modeled via eigenstrains in our finite-element model, which are provided as an external input to the system only during the photoactuated state. To do so, we add the contribution of the eigenstrains directly to the internal virtual work expression [45]. The photoinduced bending curvature can be directly correlated to the internal microstructure of the liquid-crystalline polymer and the intensity of the light

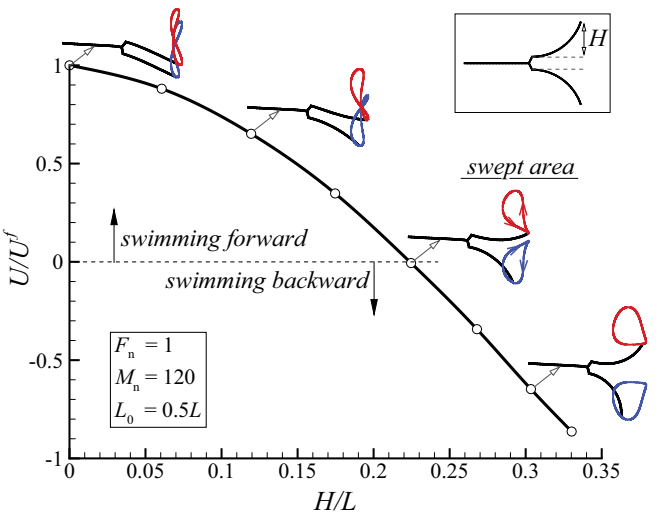

FIG. 10. (Color online) Simulation results showing the influence of the effective mastigoneme's height H (formed by the photoresponsive, nonmagnetic portion of the PME; see the inset) on the swimming velocity of a fully responsive PME, where U^f is the swimming velocity of the PME in the absence of the photoactuation. The light-actuated appendages sweep a nonzero area, which increases with H/L, leading to the swimming direction reversal [25]. The swimming direction is reversed when $H/L > 0.22$, where L is the initial length of the microswimmer.

source [29,30]. To account for this, we use representative bending curvatures to represent the deformed configuration of the photoresponsive section as illustrated in Fig. 10. We have explored the influence of the light-induced curvature (in terms of the effective mastigoneme height H; see the inset) on the swimming velocity for the fully responsive microswimmers in Fig. 10. It can be noted that the light-actuated appendages sweep a nonzero area, which increases with H/L, leading to swimming direction reversal for a critical value of H ($H/L \approx 0.22$). A similar change in swimming direction was observed for flagella covered by multiple mastigonemes [25].

IV. CONCLUSION

We have analyzed the swimming hydrodynamics of magnetically actuated artificial flagella (termed PME) using a computational approach in which the coupled magnetostatic, fluid dynamic, and solid mechanics equations are solved simultaneously. We have identified the key dimensionless parameters that can be used as a guideline to achieve an optimal (maximum) swimming velocity. It has been observed that the magnetoresponsive microswimmers become fully responsive to the applied magnetic field when $M_n > 70F_n$. Also, the role of F_n and L_0/L on the swimming velocity is explored, showing that the swimming velocity is maximal for $(L_0/L)_{opt} = 0.55$ and $F_n = 1.5$. These results allow optimal magnetic artificial flagella to be designed for a given fluid viscosity subject to the PME manufacturing constraints.

The bidirectionality of the microswimmer is addressed by proposing photoresponsive liquid-crystalline polymers for the nonmagnetic portion (or portions) of the microswimmer as an additional actuation mechanism. By controlling the phase lag between the two actuation mechanisms (magnetic field and light), the swimming direction can be reversed. This generic conceptual design is expected to be applicable to other material systems and physical actuation mechanisms as well.

Finally, the bidirectionality was demonstrated through a bioinspired approach in which the photoresponsive nonmagnetic sections mimic natural mastigonemes that act as cilia. Such a microswimmer can be easily manufactured with state-of-the-art polymer processing technologies such as inkjet printing and can potentially be used for various biomedical applications such as micro-object manipulation in laboratory-on-a-chip devices.

ACKNOWLEDGMENTS

We would like to acknowledge the Dutch Polymer Institute for funding under Project No. DPI-699 (ARTFLAG). Also, discussions with Professor D. J. Broer (TU/e) and Professor J. M. J. den Toonder (TU/e and Philips) are gratefully acknowledged.

APPENDIX A: COMPUTATIONAL MODEL

We follow the same approach as in Ref. [27], where we linearize and discretize the principle of virtual work to arrive at the final set of equations by adopting an updated Lagrangian framework. The microswimmer is represented by a collection of 2D beam elements, which act as an internal

boundary to the fluid domain. A monolithic approach is used to couple the Lagrangian formulation of the solid to the Eulerian formulation of the fluid, where we incorporate the fluid drag forces using the method of Lagrange multipliers [38]. During the simulations the external magnetic actuation leads to the generation of magnetic body couples that are considered as an external force vector to the FSI model. The magnetic body couples are obtained by solving the Maxwell equations for the magnetostatic problem with no free currents [39]. Here we briefly summarize the computational framework; for full details of the approach and validation studies the reader is referred to Ref. [27].

1. Magnetostatics

For a superparamagnetic film of length L and thickness h with magnetic susceptibility $\hat{\chi}_x$ and $\hat{\chi}_y$ in the local x and y coordinates, the out-of-plane magnetic body couple N_z can be written as [27]

$$N_z = \frac{\mu_0 H_{\text{ext}}^2 \sin(2\Theta)(\hat{\chi}_x - \hat{\chi}_y + \hat{\chi}_x\hat{\chi}_y(\beta-\alpha))}{1+\alpha\beta\hat{\chi}_x\hat{\chi}_y + \alpha\hat{\chi}_x + \beta\hat{\chi}_y}, \quad \text{(A1)}$$

where Θ is the angle between the magnetic field vector and the film, μ_0 is the permeability of free space, $\alpha = 2\tan^{-1}(h/L)/\pi$ and $\beta = 2\tan^{-1}(L/h)/\pi$ are positive factors that depend on the geometry of the film, and H_{ext} is the magnitude of the applied external magnetic field. It clearly indicates that the magnetic couple N_z is directly proportional to the square of the applied magnetic field.

2. Finite-element formulation of the solid mechanics equations

The principle of virtual work ($\delta W_{\text{int}}^{t+\Delta t} = \delta W_{\text{ext}}^{t+\Delta t}$) for the microswimmer under consideration can be written as

$$\int_V \sigma\delta\epsilon dV = \int_A (\delta\boldsymbol{u})^T \boldsymbol{T}_d dA + \int_{V_{\text{m}}} N_z \frac{\partial\delta v}{\partial x} dV_{\text{m}}, \quad \text{(A2)}$$

where σ is the stress at point (x,y), ϵ is the corresponding strain, $\boldsymbol{T}_d = \{T_u, T_v\}^T$ is the surface traction vector due to viscous forces of the fluid, V_{m} is the magnetic portion of the swimmer, and N_z is the magnetic body couple in the out-of-plane direction. The deformation of a 2D beam structure can be described in terms of the axial and transverse displacements of its axis $\boldsymbol{u} = \{u,v\}^T$. We use the finite-element formulation to discretize the system in terms of the nodal displacements and rotations $\boldsymbol{d}$ of the Euler-Bernoulli beam elements [46] of uniform cross section $A = bh$, where h and b are the thickness and out-of-plane width, respectively. After the standard finite-element assembly the discretized form of the solid's virtual work equation can be written as [27]

$$\delta\boldsymbol{d}^T\left(\boldsymbol{K}^t\Delta\boldsymbol{d} + \boldsymbol{F}_{\text{int}}^t - \boldsymbol{F}_{\text{ext}}^{t+\Delta t}\right) = 0, \quad \text{(A3)}$$

where $\boldsymbol{K}^t$ is the elemental stiffness matrix, $\boldsymbol{f}_{\text{int}}^t$ is the internal nodal force vector, and $\boldsymbol{f}_{\text{ext}}^{t+\Delta t}$ is the external force vector, which consist of tractions imposed by the fluid and the magnetic torques due to external actuation [27].

3. Formulation of the fluid dynamics equations

The principle of virtual work in rate form for the fluid problem can be written by neglecting the inertial terms [47] as

$$\int_V \sigma_{ij}\delta D_{ij} dV + \int_V \delta p \frac{\partial u_i}{\partial x_i} dV = 0, \quad \text{(A4)}$$

where σ_{ij} and D_{ij} represent the components of the stress tensor and the deformation rate tensor in the fluid, respectively, u_i represents the components of the fluid velocity in the ith direction, p is the pressure, and $dV = bdxdy$. The first term represents the work due to the internal stresses in the fluid while the second term imposes the incompressibility condition. Note that u (without a subscript) represents the axial displacement of a point on the beam (see Sec. IV), while u_i (with a subscript) represents the fluid velocity. The constitutive relation for the fluid is $\sigma_{ij} = -p\delta_{ij} + 2\mu D_{ij}$, where δ_{ij} is the Kronecker delta and μ is the fluid viscosity. The discretized form of the fluid's virtual work equation can be written as [27]

$$\delta\boldsymbol{U}^T(\boldsymbol{K}^{UP}\boldsymbol{P} + \boldsymbol{K}^{UU}\boldsymbol{U}) + \delta\boldsymbol{P}^T(\boldsymbol{K}^{UP})^T\boldsymbol{U} = 0. \quad \text{(A5)}$$

4. Fluid-solid interaction using the monolithic approach

To solve the fluid-solid interaction problem, we couple the above described Lagrangian formulation of the solid to the Eulerian formulation of the fluid, where the solid beam is considered as an internal boundary to the fluid domain. The method of Lagrange multipliers [38] is used to establish the no-slip condition (e.g., the velocity of the solid is equal to the velocity of the fluid) for the fluid-solid interaction. We start by applying the constraint or no-slip condition to the fluid dynamics model, add the virtual work done by this constraint force to the solid mechanics model, and finally couple the equations so that the solid and the fluid equations of motion can be solved implicitly.

Incorporating the variation of the Lagrange multiplier λ_i times the constraint to the fluid dynamics model [see Eq. (A5)] leads to the following equations after discretization and finite-element assembly:

$$\begin{aligned} \boldsymbol{K}^{UP}\boldsymbol{P} + \boldsymbol{K}^{UU}\boldsymbol{U} + \boldsymbol{\Phi}\boldsymbol{\lambda} &= 0, \\ (\boldsymbol{K}^{UP})^T\boldsymbol{U} &= 0, \\ \boldsymbol{\Phi}^T\boldsymbol{U} - \boldsymbol{A}\dot{\boldsymbol{d}} &= 0, \end{aligned} \quad \text{(A6)}$$

where $\boldsymbol{\Phi}$ contains the shape functions used to interpolate the fluid velocity and $\boldsymbol{A}$ is a matrix that eliminates the rotational degrees of freedom from $\dot{\boldsymbol{d}}$.

Similarly, after considering the fluid drag forces contributing to the virtual work equation of the solid [see Eq. (A3)], we obtain

$$\boldsymbol{K}^t\Delta\boldsymbol{d} + \boldsymbol{F}_{\text{int}}^t - \boldsymbol{F}_{\text{ext}}^{t+\Delta t} - \boldsymbol{A}^T\boldsymbol{\lambda} = 0. \quad \text{(A7)}$$

Note that here we invoke the arbitrary nature of the virtual fields. The motion of the elastica with time is obtained by solving the above equation with appropriate initial and boundary conditions and the time integration is performed

using the trapezoidal rule for which the nodal velocities $\dot{\boldsymbol{d}}^{t+\Delta t}$ can be written as

$$\hat{\boldsymbol{K}}\dot{\boldsymbol{d}}^{t+\Delta t} - \boldsymbol{A}^T\boldsymbol{\lambda} = \hat{\boldsymbol{F}}^{t+\Delta t}, \tag{A8}$$

where $\hat{\boldsymbol{K}} = 0.5\boldsymbol{K}^t\Delta t$ and $\hat{\boldsymbol{F}}^{t+\Delta t} = \boldsymbol{F}_{\text{ext}}^{t+\Delta t} - \boldsymbol{F}_{\text{int}}^t - 0.5\boldsymbol{K}^t\Delta t\dot{\boldsymbol{d}}^t$.

Finally, combining the equations of motion for the solid [Eq. (A8) and dropping the superscript $t+\Delta t$] and the fluid [Eq. (A6)] results in

$$\begin{bmatrix} \boldsymbol{K}^{UU} & \boldsymbol{K}^{UP} & \boldsymbol{0} & \boldsymbol{\Phi} \\ (\boldsymbol{K}^{UP})^T & \boldsymbol{0} & \boldsymbol{0} & \boldsymbol{0} \\ \boldsymbol{0} & \boldsymbol{0} & \hat{\boldsymbol{K}} & -\boldsymbol{A}^T \\ \boldsymbol{\Phi}^T & \boldsymbol{0} & -\boldsymbol{A} & \boldsymbol{0} \end{bmatrix} \begin{Bmatrix} \boldsymbol{U} \\ \boldsymbol{P} \\ \dot{\boldsymbol{d}} \\ \boldsymbol{\lambda} \end{Bmatrix} = \begin{Bmatrix} \boldsymbol{0} \\ \boldsymbol{0} \\ \hat{\boldsymbol{F}} \\ \boldsymbol{0} \end{Bmatrix}. \tag{A9}$$

This set of equations is solved to obtain the velocities at the solid and fluid nodal points, the pressure in the fluid, and the Lagrange multipliers at the solid nodal points. Note that the present approach for the fluid-solid interaction is commonly referred to as the monolithic approach, as the velocity of the film and the fluid are solved simultaneously for every time increment [see Eq. (A9)].

APPENDIX B: DIMENSIONAL ANALYSIS

We use the principle of virtual work to identify the dimensionless parameters that govern the swimming dynamics of a partially magnetized flexible elastica. This gives us a systematic approach to explore the influence of all the system parameters (e.g., length, thickness, stiffness, fluid viscosity, and magnetic field) [26,27]. Assuming bending deformations (governed by the transverse displacements v) to be dominant and considering all the relevant energies in the system, we have

$$\int_0^L EI\frac{\partial^2 v}{\partial x^2}\frac{\partial^2\delta v}{\partial x^2}dx - \int_0^{L_0} N_z\frac{\partial\delta v}{\partial x}bhdx - \int_0^L T_v\delta vbdx = 0, \tag{B1}$$

where the first term represents the virtual elastic work done by the internal moments, the second term represents the virtual work done by the magnetic body couples, and the last term represents the virtual work done by the fluid drag forces. Since the film is partially magnetic, the magnetic body couple will only act on the magnetic portion L_0 of the elastica. In Eq. (B1), E is Young's modulus, $I = bh^3/12$ is the second moment of area, N_z is the magnetic body couple in the out-of-plane direction that depends on the type of magnetic material, and T_v is the surface traction due to viscous forces of the fluid in the transverse direction. We now introduce the dimensionless variables V and X such that $v = VL^*$ and $x = XL^*$, where

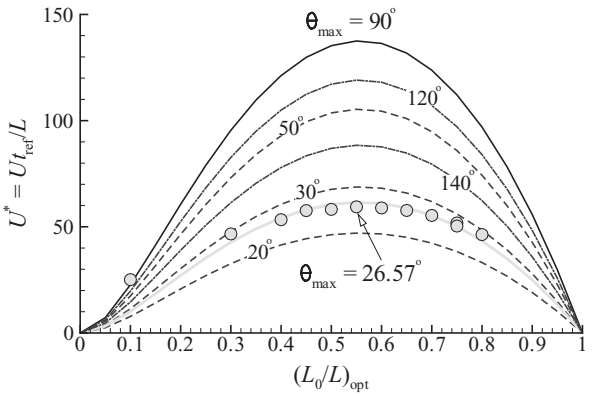

FIG. 11. For the cases of optimal swimming velocities, comparison of the analytical prediction of the swimming velocities with the simulation results (represented by the closed circles). The swimming velocity is maximal for $(L_0/L)_{\text{opt}} = 0.55$ and the corresponding value of $F_{\text{n}} = 1.5$. Note that the analytical results are scaled with a proportionality factor.

L^* is a characteristic length. Substitution yields

$$L\int_0^1 \frac{EI}{L^2}\frac{\partial^2 V}{\partial X^2}\frac{\partial^2\delta V}{\partial X^2}dX - L_0\int_0^1 N_z bh\frac{\partial\delta V}{\partial X}dX - L\int_0^1 T_v Lb\delta VdX = 0. \tag{B2}$$

It can be noted that the choice of L^* is not the same for all integrals in the above equation, which leads us to a governing dimensionless (length) parameter L_0/L defining the normalized length of the magnetic portion in the elastica. Next, normalization with the elastic term reveals the following governing dimensionless (force) parameters: (a) the magnetic number $M_{\text{n}} = N_z bhLL_0/EI$, i.e., the ratio of magnetic to elastic forces, and (b) the fluid number $F_{\text{n}} = T_v L^3 b/EI$, i.e., the ratio of fluid to elastic forces. From dimensional considerations T_v should scale with μ/t_{ref} [26,27], where μ is viscosity of the fluid and t_{ref} is the cycle time of the magnetic field oscillation. Also, for a superparamagnetic film, N_z scales with B_{ext}^2/μ_0 and depends on χ [27] [see Eq. (A1)], where μ_0 is the permeability of free space and B_{ext} is magnitude of the applied magnetic field. Thus the final form of the three governing dimensionless parameters is as follows: (i) the fraction of film that is magnetic L_0/L, (ii) the magnetic number $M_{\text{n}} = 12B_{\text{ext}}^2 LL_0/\mu_0 Eh^2$, and (iii) the fluid number $F_{\text{n}} = 12\mu L^3/Eh^3 t_{\text{ref}}$.

APPENDIX C: RESULTS

The analytical prediction of the swimming velocity based on the resistive force theory applied to an oar motion is given by

$$U^*_{\text{opt}} = U_{\text{opt}}(t_{\text{ref}}/L) \propto L_0^2(L - L_0)\sin(\theta_{\max})/(L_0L^2 + 0.2L^3)$$

(see Fig. 11).

[1] S. J. Ebbens and J. R. Howse, Soft Matter **6**, 726 (2010).
[2] L. Zhang, K. E. Peyer, and B. J. Nelson, Lab Chip **10**, 2203 (2010).
[3] E. M. Purcell, Am. J. Phys. **45**, 3 (1977).
[4] E. Lauga and T. R. Powers, Rep. Prog. Phys. **72**, 096601 (2009).
[5] E. Lauga, Soft Matter **7**, 3060 (2011).

[6] R. Dreyfus, J. Baudry, M. L. Roper, M. Fermigier, H. A. Stone, and J. Bibette, Nature (London) **437**, 862 (2005).
[7] E. Gauger and H. Stark, Phys. Rev. E **74**, 021907 (2006).
[8] A. Ghosh and P. Fischer, Nano Lett. **9**, 2243 (2009).
[9] P. Garstecki, P. Tierno, D. B. Weibel, F. Sagués, and G. M. Whitesides, J. Phys.: Condens. Matter **21**, 204110 (2009).
[10] L. Zhang, J. J. Abbott, L. Dong, B. E. Kratochvil, D. Bell, and B. J. Nelson, Appl. Phys. Lett. **94**, 064107 (2009).
[11] D. M. Woolley, R. F. Crockett, W. D. I. Groom, and S. G. Revell, J. Exp. Biol. **212**, 2215 (2009).
[12] M. C. Lagomarsino, F. Capuani, and C. P. Lowe, J. Theor. Biol. **224**, 215 (2003).
[13] C. P. Lowe, Philos. Trans. R. Soc. London Ser. B **358**, 1543 (2003).
[14] C. H. Wiggins, D. Riveline, A. Ott, and R. E. Goldstein, Biophys. J. **74**, 1043 (1998).
[15] C. H. Wiggins and R. E. Goldstein, Phys. Rev. Lett. **80**, 3879 (1998).
[16] E. Lauga, Phys. Rev. E **75**, 041916 (2007).
[17] A. A. Evans and E. Lauga, Phys. Rev. E **82**, 041915 (2010).
[18] T. S. Yu, E. Lauga, and A. E. Hosoi, Phys. Fluids **18**, 091701 (2006).
[19] S. Sudo, S. Segawa, and T. Honda, J. Intell. Mater. Syst. Struct. **17**, 729 (2006).
[20] S. Guo, Q. Pan, and M. B. Khamesee, Microsyst. Technol. **14**, 307 (2008).
[21] M. E. J. Holwill and M. A. Sleigh, J. Exp. Biol. **47**, 267 (1967).
[22] D. M. Cahill, M. Cope, and A. R. Hardham, Protoplasma **194**, 18 (1996).
[23] C. Brennen, J. Mechanochem. Cell Motility **3**, 207 (1975).
[24] M. A. Sleigh, Protoplasma **164**, 45 (1991).
[25] S. Namdeo, S. N. Khaderi, J. M. J. den Toonder, and P. R. Onck, Biomicrofluidics **5**, 034108 (2011).
[26] S. N. Khaderi, M. G. H. M. Baltussen, P. D. Anderson, D. Ioan, J. M. J. den Toonder, and P. R. Onck, Phys. Rev. E **79**, 046304 (2009).
[27] S. N. Khaderi, J. M. J. den Toonder, and P. R. Onck, Langmuir **28**, 7921 (2012).
[28] S. N. Khaderi, C. B. Craus, J. Hussong, N. Schorr, J. Belardi, J. Westerweel, O. Prucker, J. Ruhe, J. M. J. den Toonder, and P. R. Onck, Lab Chip **11**, 2002 (2011).
[29] C. L. van Oosten, K. Harris, C. W. M. Bastiaansen, and D. J. Broer, Eur. Phys. J. E **23**, 329 (2007).
[30] C. L. van Oosten, D. Corbett, D. Davies, M. Warner, C. W. M. Bastiaansen, and D. J. Broer, Macromolecules **41**, 8592 (2008).
[31] C. L. van Oosten, C. W. M. Bastiaansen, and D. J. Broer, Nat. Mater. **8**, 677 (2009).
[32] G. Taylor, Proc. R. Soc. London Ser. A **209**, 447 (1951).
[33] G. Taylor, Proc. R. Soc. London Ser. A **211**, 225 (1952).
[34] J. Gray and G. J. Hancock, J. Exp. Biol. **32**, 802 (1955).
[35] J. J. L. Higdon, J. Fluid Mech. **90**, 685 (1979).
[36] J. Lighthill, SIAM Rev. **18**, 161 (1976).
[37] R. D. Dresdner, D. F. Katz, and S. A. Berger, J. Fluid Mech. **97**, 591 (1980).
[38] C. Lanczos, *The Variational Principles of Mechanics* (University of Toronto Press, Toronto, 1952).
[39] J. D. Jackson, *Classical Electrodynamics* (Wiley, New York, 1974).
[40] See Supplemental Material at http://link.aps.org/supplemental/10.1103/PhysRevE.88.043013 for the animation of unidirectional as well as bidirectional swimming of the artificial flagella with external stimuli.
[41] R. Golestanian and A. Ajdari, Phys. Rev. E **77**, 036308 (2008).
[42] E. Lauga and D. Bartolo, Phys. Rev. E **78**, 030901(R) (2008).
[43] M. Polin, I. Tuval, K. Drescher, J. P. Gollub, and R. E. Goldstein, Science **325**, 487 (2009).
[44] E. Smith, Mol. Biol. Cell **13**, 3303 (2002).
[45] R. Annabattula, W. Huck, and P. Onck, J. Mech. Phys. Solids **58**, 447 (2010).
[46] R. D. Cook, D. S. Malkus, M. E. Plesha, and R. J. Witt, *Concepts and Applications of Finite Element Analysis* (Wiley, New York, 2002).
[47] K. J. Bathe, *Finite Element Procedures* (Prentice-Hall, Englewood Cliffs, NJ, 1996).